

**Physical defects in basement membrane-mimicking
collagen-IV matrices trigger cellular EMT and invasion**

Journal:	<i>Integrative Biology</i>
Manuscript ID	IB-ART-02-2018-000034.R1
Article Type:	Paper
Date Submitted by the Author:	30-Apr-2018
Complete List of Authors:	Walter, Christopher; Washington University in Saint Louis, Biomedical Engineering Davis, Joshua; Washington University in Saint Louis, Mechanical Engineering & Materials Science Mathur, Jairaj; Washington University in Saint Louis, Mechanical Engineering & Materials Science Pathak, Amit; Washington University in Saint Louis, Mechanical Engineering & Materials Science

Insight, innovation, integration

In fibrosis and cancer, degradation of basement membrane (BM) and cell invasion are considered as key outcomes of a cellular transformation called epithelial-mesenchymal transition (EMT).

We have discovered a reverse phenomenon in which preexisting defects in a BM-like matrix trigger EMT and invasion in normal epithelial cells, regulated by MMP9-enabled degradation of collagen-IV. In reality, such defects in the BM could arise from wounds or incisions that are otherwise regarded as benign for long-term health. Our findings reveal that physical defects in the BM can initiate the pathological cellular transformation of EMT and may commence a positive feedback loop of disease progression and BM degradation. This causal relationship between defective BM and EMT could inform new therapeutic strategies.

Physical defects in basement membrane-mimicking collagen-IV matrices trigger cellular EMT and invasion

Christopher Walter^{2,†}, Joshua T Davis^{1,†}, Jairaj Mathur¹, and Amit Pathak^{1,2,*}

¹*Department of Mechanical Engineering & Materials Science, Washington University, St. Louis*

²*Department of Biomedical Engineering, Washington University, St. Louis*

[†]*These authors contributed equally to this work.*

** To whom correspondence should be addressed:*

Amit Pathak, Ph.D.

One Brookings Dr, CB 1185, Saint Louis, MO 63130

Ph: (314) 935-7585; Email: pathaka@wustl.edu

Keywords – physical defects, epithelial-mesenchymal transition (EMT), invasion, collagen-IV matrix, basement membrane.

Abstract

In fibrosis and cancer, degradation of basement membrane (BM) and cell invasion are considered as key outcomes of a cellular transformation called epithelial-mesenchymal transition (EMT). Here, we pose a converse question – can preexisting physical defects in the BM matrix cause EMT in normal epithelial cells? On a BM-mimicking matrix of collagen-IV-coated polyacrylamide (PA) gel, we have discovered a reverse phenomenon in which preexisting defects trigger EMT in normal epithelial cells. Through spatiotemporal measurements and simulations *in silico*, we demonstrate that the EMT precedes cellular mechanoactivation on defective matrices, but they occur concurrently on stiff matrices. The defect-dependent EMT caused cell invasion through a stroma-mimicking collagen-I layer, which could be disabled through MMP9 inhibition. Our findings reveal that the known BM degradation caused by cellular EMT and invasion is not a one-way process. Instead, normal epithelial cells can exploit physical defects in the BM matrix to undergo disease-like cellular transformations.

1. Introduction

In pathogenesis of cancer and fibrosis, the epithelial integrity is compromised through an epithelial-mesenchymal transition (EMT) of cells.¹ Additionally, the basement membrane (BM) matrix is degraded as the disease conditions progress.² As a result of these cellular and extracellular malfunctions, the cells transformed by the EMT invade through the BM and into the surrounding stroma.³ Despite the known importance of the integrity of epithelial junctions and BM composition in healthy tissues, a connection between their dysfunctional transformations remains unclear.

The BM matrix is a thin and dense sheet-like network of extracellular matrix (ECM) proteins, which is connected to the basolateral side of epithelial or endothelial cells throughout mammalian organs and tissues.⁴ This membrane is essential for maintaining the health of the underlying tissue by providing structural support at the epithelium-stromal interface and serving as a barrier to foreign macromolecules.⁵ Healthy BM structure plays an important role in preventing the invasion of cancer cells into the vasculature.⁶ In breast cancer metastasis, basement membrane degradation is one of the key steps in the transformation of an *in situ* tumor into an invasive one.⁷ Collagen type IV (col-IV) is the majority constituent in the BM composition, along with laminins, heparan sulfate proteoglycans, and nidogens.^{6,8} The col-IV fibrils in the BM form a highly cross-linked network with occluded binding sites for other proteins^{9,10}. This networked col-IV prevents BM degradation and invasion of attached epithelial cells into the stromal matrix.^{2,6,11,12} However, as epithelial cells undergo EMT, they start to break cell-cell junctions, become fibroblastic, and attain motile characteristics, enabling them to deform and degrade their underlying BM; all of which are crucial early events in tumor invasion.¹ It is now known that matrix stiffness triggers EMT in epithelial cells through cellular

mechanoactivation.¹³⁻¹⁵ Furthermore, matrix topography, confinement and spatial patterning of ligands can induce EMT-like signatures in epithelial cell populations.¹⁶⁻¹⁸ These matrix-dependent mechanosensitive modes of EMT are particularly relevant for fibrosis¹⁹ and cancer,¹⁵ where mechanical properties of the tissue microenvironment undergo dramatic changes during disease progression. Thus, it is possible that physical heterogeneities in the BM could break the symmetry in normal epithelial layers and trigger similar ECM-dependent pathogenic cellular transformations.

The EMT and associated stimulation of matrix metalloproteinases (MMPs) and cellular mechanoactivation have been shown to degrade the BM matrix in wound healing,²⁰ development,^{21,22} and cancer progression.^{23,24} Aside from pathological reasons and cellular transformations, the BM matrix can also sustain damage due to physical wounds, incisions, or surgeries. Although a homogeneous soft BM matrix is known to protect the epithelial state, it remains unknown whether mechanical heterogeneities and defects in the BM contribute to pathologically-relevant cellular transformations. In this study, we ask this converse question – can preexisting physical defects in healthy and soft BM-like matrix cause EMT and invasion in normal epithelial cells? If true, this finding will reveal that the heterogeneous transformation of the BM structure during disease progression is not merely a passive outcome but an active instigator of cellular EMT.

To address this question, we fabricated a soft polyacrylamide (PA) gel, one that protects against EMT, functionalized a layer of col-IV to mimic BM-like properties, and manually introduced a tear in the gel. Given that col-IV represents the majority structural component of the BM matrix and that physical properties of the BM are the focus of our study, we chose it as the primary ECM protein for our *in vitro* BM-mimicking scaffolds. We cultured MCF10A human

mammary epithelial cells and found enhanced EMT markers around this physical matrix defect. We also measured how two different anomalies in the BM-like matrices – physical defects in soft matrix or homogeneous stiff matrix – cause EMT and cellular mechanoactivation. Through a new computational model that integrates cellular forces, cell-cell junctions, mechanoactivation and EMT in a multi-cell network, we simulated the spatiotemporal evolution of EMT progression and cellular mechanoactivation around the defect. Through a novel 3D scaffold combining both BM-like and stroma-like matrices, we showed that the defect-induced EMT not only persists in 3D, but also causes downward cell invasion. These findings demonstrate that the known degradation of BM caused by cellular EMT and invasion³ might not be a one-way process. Instead, our results reveal a previously unidentified ability of normal epithelial cells to exploit the physical defects in the BM matrix to attain EMT and invasive phenotypes.

2. Methods

Fabrication of collagen IV-coated PA gels with defect.

Glass coverslips were activated by plasma cleaning and Bind-Silane solution (94.7% ethanol, 5% acetic acid, and 0.3% Bind-Silane). After 10 minutes, the coverslips were washed in ethanol and air dried. Polyacrylamide gels were synthesized by free-radical polymerization according to protocols previously established.²⁵⁻²⁷ Precursor solutions combining acrylamide, bis-acrylamide, and ultrapure water were mixed at a ratio of 10%, 0.15%, and 89.85% respectively for ~50 kPa and 4%, 0.2%, 95.8% for ~0.5 kPa stiffness, as characterized before²⁵ and confirmed here (Fig. 1). A solution of 10% ammonium persulfate was added along with N,N,N',N'-tetramethylethylenediamine (TEMED) at 1:200 and 1:2000 v:v, respectively. Polyacrylamide solution was applied to the activated coverslips using a Sigmacote (MilliporeSigma, St. Louis,

MO) treated microscope slide and allowed to polymerize for 30 minutes. Formed gels were functionalized with 0.5 mg/mL solution of sulfosuccinimidyl 6-(4'-azido-2'-nitrophenylamino) hexanoate (Sulfo-SANPAH) (Thermo Fisher Scientific) prepared in 50mM HEPES buffer (Santa Cruz Biotechnologies) and crosslinked to the PA surface upon activation with 365 nm UV for 10 minutes. Gels were then washed 3 times before applying a 0.5 mg/mL solution of type-IV collagen from human placenta (col-IV) (Millipore Sigma, St. Louis, MO). After col-IV application, coverslips were placed at 4°C overnight (<12 hours), then washed. A scalpel was used to make an incision 1 cm in length immediately prior to cell addition. Cells were plated onto gels within 24 hours of col-IV deposition.

Cell Culture.

MCF-10A cells were cultured in DMEM/F12 supplemented with 5% horse serum, 0.2% Normocin, 20 ng/mL EGF, 0.5 mg/mL hydrocortisone, 100 ng/mL cholera toxin, and 10 µg/mL insulin, as previously established.^{25,28,29} Media was changed every 3 days. For MMP9 inhibition experiments, cells were treated with the MMP9 Inhibitor (CAS 1177749-58-4; Calbiochem) at 5 nM concentration. Efficacy of the MMP9 Inhibitor was performed using an MMP9 inhibitor Screening Assay from Abcam (ab139449) according to assay protocol (details provided with Fig. S7).

Immunofluorescence and Image Analysis.

After 1, 3, or 6 days of culture, the cells were fixed with 4% Paraformaldehyde for 10 minutes, washed, and permeabilized using 0.1% solution of Triton X-100 for 15 minutes. Cells were washed again and non-specific binding was blocked by 3% Bovine Serum Albumin (BSA)

solution in PBS containing 0.1% Tween-20 for one hour. Primary antibody solutions were incubated overnight at 4°C. Secondary antibody solutions were incubated for one hour at room temperature. Primary antibodies used were against col-IV (1:500; Abcam), MMP9 (1:500; Invitrogen), E-Cadherin (1:200; Cell Signaling), pMLC (1:500; Invitrogen) and Vimentin (1:750; Pierce Biotech). Secondary antibodies used were goat anti-rabbit Alexa 647 (1:300; Life Technologies) and goat anti-mouse Alexa 488 (1:300; Life Technologies). F-actin was stained using rhodamine phalloidin (1:400; Life Technologies). Once stained, coverslips were mounted in Slowfade Diamond with DAPI (1:250; Life Technologies) onto microscope slides and sealed with a number 1.5 coverslip. Images were taken using an Olympus FV1200 scanning laser confocal microscope using an UAPON 40XW340 objective. Unless otherwise specified, all experiments were carried out with 3 experimental replicates and at least 6 technical replicates. Image analysis was performed using FIJI. E-cadherin membrane localization was calculated by dividing the E-cad expression on the cell membrane by the total E-cad expression to obtain a normalized ratio for each cell. Quantification of vimentin, pMLC, and col-IV was performed by measuring the pixel intensity per unit area in images with a cell monolayer present and only in areas in which cells were present (areas beyond the defect were not considered in the calculations). To quantify actin fiber formation, the average background intensity across all conditions was calculated and subtracted from each image, leaving behind only the high intensity actin stress fibers. Pixel intensity was then calculated from these images. To account for discrepancies in cell number and monolayer area, only data from full, unbroken areas of the monolayer were considered and all data were normalized by the area measured. Long-distance vimentin images were obtained by imaging gel constructs with complete monolayers that extended >3 mm from the induced defect. Images were acquired in tiles using a laser-scanning

confocal microscope (Zeiss LSM 810; Carl Zeiss MicroImaging; Germany) using a 40X objective and stitched together using ZEN2.1 software.

Fabrication of multi-layered 3D matrices and invasion analysis.

To measure 3D cell invasion around the defect, a 3D ECM was fabricated by layering a coating of BM-mimicking col-IV on top of a matrix of stroma-mimicking Rat Tail Type I collagen (col-I; Santa Cruz Biotechnology). First, polyacrylamide gels were synthesized on coverslips and treated with Sulfo-SANPAH as with the aforementioned 2D substrates, after which 50 μ L of col-I at a concentration of 0.5 mg/mL was applied and allowed to polymerize for 1 hour at 37°C. After the col-I layer had polymerized, a 0.5 mg/mL concentration col-IV solution was applied and allowed to polymerize overnight at 4°C. A crack was introduced after at least 12 h incubation. Cells were then seeded as a monolayer on the PA/col-I/col-IV layered scaffold and the cells were allowed to grow for 6 days. For immunofluorescence imaging, a similar procedure compared to the procedure used for the 2D gels was used here. A primary antibody against type-I collagen (Abcam) was used for staining the col-I matrix. Images were obtained using the Zeiss LSM 810 confocal microscope with 2 μ m thick z -stacks. Invasion cell counts were obtained by counting the number of whole nuclei present within the 2 μ m stack. Cell counts were also divided into 100 μ m sections measured from the defect.

qPCR.

Cells were grown on gels that contained 5 defects, spaced 3 mm apart, in order to maximize the number of cells exposed to the network break. These multiple cut gels were used for extracting mRNA for qPCR analyses. mRNA was extracted using Qiagen Quick RNA extraction kit

(Qiagen) according to manufacturer's instruction. Primers for SNAI1, Zeb1, PTEN, and RRNA18 (Qiagen) were used and experiments were performed using SYBR green (Qiagen). Results were normalized and evaluated by geometric mean outlined by Livak & Schmittgen.³⁰

AFM.

Atomic Force Microscopy (AFM) measurements of polyacrylamide gels were made using an MFP-3D-BIO atomic force microscope (Asylum Research, Santa Barbara, CA). Olympus TR400PB AFM probes with an Au/Cr coated silicon nitride cantilever and pyramidal tip were used, with spring constants ranging from 20-30 pN/nm as measured by thermal calibration (Asylum Research, Santa Barbara, CA). 50 μm x 50 μm force maps were taken at the location of the defect (<200 μm), away from the defect (>2 mm), and on control substrates, with 100 points per force map. Elastic moduli were extracted from force curves using a modified Hertz model, as described earlier.³¹

Statistical Analysis.

Unless specified otherwise, results are reported as the mean \pm Standard Error (SE). To identify the significant differences between two experimental conditions, an *F*-test was performed to determine whether equal variance could be assumed. Next, Student's *t*-test was used to determine significant differences between two groups. All statistical analyses were performed using the Data Analysis toolbox in Microsoft Excel. Differences were considered to be significant for $P < 0.05$.

Computational Model.

To investigate the effects of a discontinuity or defect in a col-IV based ECM of defined stiffness, we developed a model that integrates subcellular signaling of mechanoactivation and cell-cell junctions with cell-level deformations and epithelium-level propagation of these signal in a spatiotemporal manner. Here, the epithelial cell monolayer is modeled through a vertex dynamics model in a CHASTE framework in which each cell is represented as a polygon.^{32,33} A collection of these polygonal cells is referred to as a “mesh”, which is comprised of a set of “elements” and “vertices”, wherein each vertex is defined as points that move in time and space. Forces act only upon these vertices, and under the assumption of overdamped motion of vertices.³⁴ By treating the entire cell monolayer at the same height, the equation of motion for any vertex ‘ i ’ is written as

$$\frac{dr_i}{dt} = \frac{F_i}{\mu} , \quad (1)$$

where r_i is the position of the ‘ i ’th vertex and F_i is the total force acting on this vertex. $\mu = 0.05$ is the damping constant.

The net force on any vertex has two contributions: active and passive. The passive forces arise due to cellular deformations, and are modeled by minimizing the free energy contributions from cell body and cell membrane. The free energy E for an element ‘ j ’ is given by:³⁵

$$E_j = \frac{K_j}{2}(A_j - A_j^0)^2 + \frac{\Gamma_j}{2}(P_j)^2 + \sum_{m=0}^{n_k-1} \Lambda_{j,m} d_{j,m} \quad (2)$$

Here, the first term represents cell elasticity, with K_j representing elastic constant, A_j and A_j^0 representing the actual and target cell areas, respectively. Second term represents the supracellular

actin-myosin ring contractility, where Γ_j is a proportionality constant and P_j is the perimeter. The third term represents line tension $\Lambda_{j,m}$ at the junctions between element j and its n_k neighbors, and $d_{j,m}$ is the corresponding shared edge length. Edges of an element that are not shared by a neighboring cell element, i.e., for cells at the monolayer boundary or ECM discontinuity, can have a different line tension. The values of these parameters corresponding to ‘passive’ properties of the cell are kept constant for all elements: $K_j = 5$, $A_j^0 = 1$, $\Gamma_j = 0$. The line tension Λ_{ij} for an edge at the interface of neighboring elements ‘ i ’ and ‘ j ’ who share a common edge is written as:

$$\Lambda_{ij} = \frac{(\beta_i + \beta_j)}{2} + C \quad (3)$$

where the line tension depends on the normalized cell-cell connections made by a cell, β_j (discussed further). $\Lambda_{j,interior} = \Lambda_{j,boundary}/2$, with ‘interior’ referring to cells within the monolayer and ‘boundary’ for cells at the periphery, respectively. $C = 0.06$ is a constant.

Thus, the passive force acting on each vertex ‘ i ’ is given by:

$$F_{passive,i} = -\nabla_i \sum_{j \in N_i} E_j, \quad (4)$$

where N_i denotes the set of elements that contain vertex ‘ i ’.

As cells in the cluster interact with one another, their physical interaction with the ECM is also maintained through cell-ECM adhesions. The active cellular forces are a result of these cell-ECM interactions. These active forces are proportional to subcellular mechanoactivation signal ϕ , written as:

$$F_{a,i} = \begin{cases} \sum_{j \in N_i} \left(\frac{K\phi_j |\vec{r}_i \cdot \hat{P}_j|}{\sum_{i \in m_j} |\vec{r}_i \cdot \hat{P}_j|} \right), & \vec{r}_i \cdot \hat{P}_j \geq 0 \\ 0, & \vec{r}_i \cdot \hat{P}_j < 0 \end{cases} \quad (5)$$

Here, $F_{a,i}$ is the active force on a node ‘ i ’, N_i is the set of elements contained by node ‘ i ’, m_j are the vertices that are in the “front” of the cell ‘ j ’, with respect to its polarization direction \hat{P}_j and ϕ_j is the mechanoactivation. The “front” of the cell ‘ j ’ is defined with respect to the polarization such that any given vertex ‘ i ’ lies in the front of the cell if $\vec{r}_i \cdot \hat{P}_j \geq 0$.

Through integrin-cadherin crosstalk, the cells are known to upregulate their force-generating mechanoactivation upon EMT induction,^{16,36,37} which we capture as the loss of cell-cell junctions. Thus, the mechanoactivation signal for a cell ‘ j ’ is dependent on the cell-cell connections made by the cell as follows:

$$\frac{d\phi_j}{dt} = r_\phi(\phi_m - \phi_j) + r_{\phi\beta}(1 - \beta_j) \quad (6)$$

where β is the normalized number of cell-cell junctions each cell. $r_\phi = 0.015$ and $r_{\phi\beta} = 0.05$. ϕ_m is defined to be the contribution to mechanoactivation directly from ECM stiffness, which can increase based on the integrin-cadherin crosstalk:

$$\phi_m = \max(m) * (1 - \beta) + m\beta \quad (7)$$

Here m is the scaled contribution from stiffness, written here as:

$$m = m_0(1 - e^{-E/E_0}) \quad (8)$$

where $E_0 = 10$ and $m_0 = 20$ are calibrated constants.

For each cell, the number of cell-cell junctions are dependent upon the feedback from the mechanoactivation signal. Additionally, the presence of a defect leads to the degradation of col-IV, which upon diffusion, causes a dissociation of cell-cell junctions. These effects are combined as following:

$$\frac{d\beta_j}{dt} = -r_\beta \phi_j^2 \beta_j \left(1 - \frac{l_j}{l_0}\right) - r_\psi \psi_j \beta_j \quad (9)$$

Here, $r_\beta = 0.0015$, $r_\psi = 0.01$ are constants. l_j is the cell-cell contact length for the cell 'j' and $l_0 = 10$ is a constant. ψ_j is the col-IV level at the cell 'j' and is modeled as a moving line source causing diffusion. It is based on the idea that degraded col-IV (ψ_j) diffuses through the epithelial layer at certain spatiotemporal rates and cause EMT, calibrated against experimental findings of EMT propagation as following:

$$\psi_j(x_j, t) = \begin{cases} 1/(1 + (x - vt)/x_\psi)^2 & , \quad t < t_\psi \\ 1 & , \quad t \geq t_\psi \end{cases} \quad (10)$$

Where v is the speed of col-IV degradation away from the defect, t is current time, x_j is the perpendicular distance of the centroid of cell 'j' from the defect, $t_\psi = x_j/v$ is the time taken for the col-IV level to achieve its maximal level ($\psi = 1$) at distance x_j , and $x_\psi = 1 \text{ mm}$ defines the zone of influence due to col-IV diffusion from the source (any location with $\psi = 1$) at time 't'.

These subcellular models were integrated with the CHASTE software to simulate the response of multi-cell networks of defined dimensions in the three ECM conditions investigated in experiments – soft homogeneous ECM, soft ECM with a defect/discontinuity on one side, and a stiff homogeneous ECM. Commensurate with the size of monolayer in experiments, we use a

monolayer with 200 cells in length, assuming average cell diameter to be $\sim 10 \mu\text{m}$, which yields a 2 mm long epithelial layer (Movie S1, top panel). The network is 6 cell-lengths wide, with periodic boundary conditions imposed on the horizontal edges to represent an infinite sheet in the vertical direction. The same ‘infinite-sheet’ boundary condition is used on the right vertical edge of the monolayer. For the soft-defect case, the monolayer is assumed to be discontinuous, i.e., without the infinite boundary condition, on the left side. Simulation time is 144 hours (6 days) to match the experiments. Initial values of $\phi = 0.1$ and $\beta = 1$ is applied for all cells. The governing equation for node displacement (Eq. 1) is solved using the explicit Forward Euler discretization method, with time step $dt = 0.001$. Differential equations for ϕ and β (Eqs. 6, 9) are solved using the implicit Runge-Kutta method. The direction of polarization \hat{P} is evaluated to be in a random direction for each cell, which changes at 1 h time interval.

3. Results

3.1. Preexisting defect in collagen IV-coated soft matrix induces EMT in epithelial monolayer.

To culture cells on a BM-like substrate, we fabricated PA hydrogel substrates of defined stiffness, prescribed through ratios of monomer and crosslinker,^{17,26,27} and of at least $100\mu\text{m}$ thickness on a glass coverslip (Fig. 1A). We picked a low PA stiffness of $\sim 0.5 \text{ kPa}$, because it preserves the epithelial state of the cell monolayer in control matrix settings (homogeneous gel without defects). It is important to perform measurements of defect-induced EMT on soft substrates, because stiff ECMs are known to induced EMT through activation of the TGF- β signaling pathway, regardless of matrix topography or structure.^{13,15-17,19} Next, we functionalized

the PA gel surface and coated a layer of 0.5 mg/ml col-IV, which is a majority ECM protein in the BM matrix. Afterwards, we introduced a tear in the soft PA gel as described in Methods, resulting in an average defect width of $\sim 40\mu\text{m}$ width (Figs. 1A,B,D). Through Atomic Force Microscopy (AFM), as done previously,^{26,31} we verified that the introduced physical defect in the PA gel does not cause significant change to its stiffness (Fig. 1C). Since only the top surface of the PA is functionalized and coated with protein, the inner surfaces of the defect remain uncoated, prohibiting any attachment to the inside walls of the defect. By comparing col-IV images before and after introducing the defect (Fig. S1), we verified that cutting the gel does not create an aligned pattern of col-IV along the defect, which could have introduced an additional topographic cue. In rare cases, if some col-IV lands within the valley of the defect, any cells within the defect (near the bottom surface) are unable to interact with the cell monolayer cultured on top of the PA gel (Fig. S2).

On soft col-IV-coated PA gels, both with and without defect, we cultured MCF10A cell monolayers for 3 days. After fixing the samples, we stained and imaged for E-cadherin (an epithelial marker) and vimentin (a mesenchymal marker). For control measurements, we repeated experiments on homogeneous, i.e., without a defect, PA gels of the same stiffness. We observed a nearly 4-fold increase in vimentin expression due to the presence of the defect (Figs. 2A,B; Fig. S3), a reduction in E-cad membrane localization by $\sim 35\%$ (Figs. 2A,C; Fig. S3), and a rise in cell spreading and elongation (Figs. 2D,E), all of which are signatures of EMT. We also imaged for col-IV near the gel surface in each condition and found that the level of col-IV around the defect decreased by $\sim 50\%$ compared to the homogeneous substrates, which indicates col-IV degradation occurring concurrently with EMT induction (Figs. 2F, S4). To confirm EMT through molecular analyses, we extracted mRNA from MCF10A cells on gels with and without

defects and performed qPCR. We chose primers for SNAIL, ZEB1, PTEN, and RhoA as a marker for cell mechanoactivation. We found that the levels of SNAIL (SNAI1) and ZEB1, both of which are hallmark transcriptional factors for EMT, increased over two-fold (Fig. 2G). We also found that PTEN level, which dephosphorylates PI3K^{38,39} to maintain epithelial phenotype, was reduced by ~50%. Surprisingly, the RhoA activation remained undetectable and similar to the control soft gels, even as the EMT markers were enhanced after 3 days of culture on defective gels. These findings show that physical defects in col-IV-coated soft matrices can induce EMT in normal epithelial cells within 3 days of culture without a prior RhoA-based cellular mechanoactivation.

3.2. Stress fiber formation on soft col-IV matrices rises after defect-induced EMT, but more rapidly and concurrently with EMT on stiff matrices.

To measure the chronological sequence of EMT and stress fiber formation, a signature of cellular mechanoactivation, we compared the expressions of aligned F-actin fibers, phosphorylated myosin light chain (pMLC), and vimentin after 1, 3, and 6 days of cell culture on the defective soft matrix (Fig. 3). Cells cultured for only 1 day on soft or defective soft matrices showed low vimentin expression (Fig. 3,S5A). After 3 days, however, vimentin expression on defective soft matrices increased by over 3-fold compared to day1 and by nearly 4-fold compared to the homogeneous soft matrices, continuing to increase by another ~50% over 6 days (Fig. 3B,S5A). In contrast, for the soft-defect case, the expression of actin fibers remained low in the first 3 days and then rose by more than 5-fold over 6 days (Fig. 3A,C). Since stress fiber activity combines both actin and myosin expressions, we also measured pMLC expression (Figs. 3D, S5B), which followed trends similar to the actin fiber formation and vimentin expression.

Since the matrix-dependent EMT has conventionally been associated with matrix stiffening,^{15,17,19} we compared EMT and stress fibers on col-IV-coated homogeneous (without defect) stiff matrices of ~50 kPa Young's Modulus (Fig. 1C). We found that vimentin expression, pMLC, and actin fibers increased by the first day in culture and stayed high over 6 days of culture (Figs. 3A-D; S5). These results indicate that soft col-IV matrix requires a defect to induce EMT, but sufficiently stiff matrix does not. To test whether slight stiffening of the matrix can trigger EMT in the absence of defect, we repeated these measurements after 3 days of culture on a col-IV coated PA gel of ~1.3 kPa stiffness, which is over three-times the stiffness of the control soft matrix, and found that vimentin expression and stress fiber formation remained at the low levels observed for the control soft matrix (Fig. S6).

These temporal results highlight that the defective soft col-IV matrix first induces EMT within the first 3 days, which is followed by broad cellular mechanoactivation and further surge of EMT over 6 days. In contrast, on the stiff matrix, cellular mechanoactivation and EMT occur both rapidly and somewhat concurrently, with increased stress fiber formation and EMT markers within 1 day, followed by a continued rise over 6 days.

3.3. Inhibition of MMP9 disables col-IV degradation and defect-induced EMT.

Since EMT signatures rose without significant cellular mechanoactivation (stress fibers and RhoA activity) within 3 days for the soft-defect case, we sought to investigate other factors associated with the defective col-IV matrix. Earlier, we found a reduction in col-IV expression on the defective matrix compared to the homogeneous substrates (Figs. 2F, S4), which indicated cellular degradation of col-IV, enabled by the mechanically introduced defect. Given that MMP9 is known to play a crucial role in degradation of col-IV,⁴⁰ we repeated our measurements

after treating the cells with a pharmacological inhibitor of MMP9. The efficacy of the inhibitor was confirmed using an MMP9 inhibitor assay kit (Abcam), as shown in Fig. S7. As expected, treatment with MMP9 inhibitor resulted in a loss of col-IV degradation on defective soft matrices (Fig. 4B, S9). The MMP9-inhibited cells showed dramatically reduced EMT markers, including vimentin expression and levels of SNAIL, ZEB1, and enhanced epithelial markers such as E-cad expression and PTEN levels compared to the untreated controls (Figs. 4, S8). As a result, the MMP9-inhibited cells lacked expression of EMT markers in both soft-homogeneous and soft-defect matrix conditions. The RhoA activation continued to remain low in MMP9-inhibited cells (Fig. 4G). Notably, the MMP9-inhibited cells persisted to express robust EMT signatures on stiff matrices (Fig. 4, S8), which shows that the selected MMP9 inhibitor is not a generic blocker of EMT. In other words, the loss of the ability of cells to degrade col-IV disabled their sensitivity to the physical defect in the col-IV soft matrix and the cells only responded to the changes in matrix stiffness.

3.4. Computational modeling of defect- and stiffness-induced EMT through a vertex-based multi-cell network.

Our experimental results point to a conceptual model for spatiotemporal evolution of EMT and mechanoactivation triggered by ECM stiffness or defect. To better integrate these intercoupled processes within a consistent mathematical framework, we devised a computational model by utilizing a vertex dynamics model (see details and governing equations in Methods). Briefly, we modeled a cell monolayer using the CHASTE framework in which each cell is represented as a polygon^{32,33}. Both the active and the passive cellular forces are applied on the vertices of these cell elements. While passive forces depend on the spatial arrangement of the cell elements, the

active forces are proportional to a mechanotransductive signal ϕ due to direct sensing of ECM stiffness through focal adhesions. The temporal variation of the mechanoactivation also depends on cell-cell junctions β , which themselves are regulated by both the mechanoactivation and the concentration of degraded col-IV.

To calibrate the modeling constants corresponding to spatiotemporal rates and gradients against key experimental observations of EMT evolution, we measured and plotted vimentin expression as a function of distance from the defect after 3 and 6 days (Fig. 5A). After 3 days, the vimentin expression significantly diminished beyond 500 μm from the defect. However, after 6 days of culture, the vimentin expression remained consistently high up to 2 mm away from the defect, and only slightly decreased beyond 2 mm. After calibrating the rate constants, we performed simulations in which cells within a 2 mm long epithelial layer, with semi-infinite boundaries along the width, achieve mechanoactivation, undergo deformation, and lose cell-cell junctions based on the model. In the case of a soft col-IV ECM with defect on one side, the EMT induction was calculated as the loss of cell-cell junctions $(1 - \beta)$ over 6 days and as a function of distance from the defect. Up to at least the 4-day mark, the calculated EMT induction $(1 - \beta)$, which may be compared with experimental measurements of vimentin expression (Fig. 5A), was significantly higher near the defect and subsided away from the defect (Fig. 5B). Over 5-6 days, the EMT signal spread through the whole monolayer. These calibrations indicated that the choice of model parameter $v = v_o = 1.67 \mu\text{m}/\text{h}$, which corresponds to the speed of col-IV degradation, correctly simulates the experimentally measured spatiotemporal profile of EMT induction (vimentin expression). We also calculated the mechanoactivation signal ϕ , which is responsible for cellular forces and has an antagonistic relationship with cell-cell junctions β ,¹⁶ and found its quick rise near the defect, which is caused by the high EMT signal and

discontinuity boundary condition near the defect (Fig. 5C). According to our simulations, the EMT signal rises such that it precedes the mechanoactivation signal near the defect over time (Fig. 5D).

Next, we repeated these simulations for epithelial layers on homogeneous, without any discontinuity, ECMs of 0.5 and 50 kPa stiffness. Consistent with the experimental results (Figs. 2, 3), we plotted the EMT and mechanoactivation signals corresponding to 3 and 6 days of simulation time and for the three main ECM conditions – soft homogeneous, soft with defect, and stiff homogeneous (Figs. 5E,F). Although soft homogeneous ECM did not cause the rise of EMT and mechanoactivation signals, the defect condition led to high EMT signal due to the degradation of col-IV, followed by a steady rise in mechanoactivation over 6 days. On the stiff homogeneous ECM, both EMT and mechanoactivation rise quickly within 3 days and reaches their maximum value over 6 days. Through the visualization of representative snapshots of cell elements in Figs. 5G and S10 (along with Movies S1-3 for spatiotemporal evolution of EMT), we show that cell elements deform and elongate as EMT and mechanoactivation rise in soft-defect and stiff conditions, which is also in agreement with experimental findings.

One of the key parameters in the model is the spatial velocity $v = v_o$ of col-IV degradation away from the defect, which results in the observed temporal EMT responses (Fig. 5). Although it would be quite difficult to control and tune this parameter in the experiments, it is conceivable that the rate of col-IV degradation *in vivo* might vary according to numerous factors, including tissue context, cell types, or the presence of other ECM proteins. To better understand the influence of this col-IV degradation speed on the spatiotemporal EMT response, we performed calculations for varying degradation velocities and found that slower col-IV degradation can restrict the defect-induced EMT within the defect vicinity in the short term (day

3 in Fig. 5H). However, our calculations show that over 6 days, col-IV released from the defect eventually diffuses through the entire monolayer and causes a broad EMT response, which happens because the zone of influence of the defect is still quite wide (defined by $x_\psi = 1 \text{ mm}$). To control the distances over which col-IV can diffuse from the defect, we varied x_ψ while keeping the spatial velocity of degradation at zero. Our calculations show that lowering the values x_ψ further restricts the defect-induced EMT closer to the defect (Fig. 5I), dropping to negligible levels when restricted only to the first row of cells at the defect ($x_\psi = 10 \mu\text{m}$).

3.5. Defect-induced EMT leads to 3D cellular invasion through collagen I matrix.

An important biological consequence of EMT is the increased cellular invasion into the surrounding matrix, specifically stromal invasion in cancer cell metastasis.¹ To test whether the defect-induced EMT and cellular mechanoactivation causes these cells to invade in a 3D environment, we created a multi-layered gel substrate by first synthesizing a type-I collagen (col-I) gel on top of soft PA gels, then depositing a layer of col-IV on top of the col-I gel (Fig. 6A). It is important to use a soft PA gel as a foundation for this system, otherwise the cells might sense underlying stiff glass,^{41,42} which is different from the conditions present *in vivo*. As before, we introduced a defect in the col-IV/col-I gel and seeded a cell monolayer on top. After 6 days of culture, we performed confocal microscopy to image for cells within the 3D col-I matrix, which showed extensive invasion of cells underneath the monolayer (Fig. 6B; Movie S4). We counted the number of cell nuclei within 5 μm thick confocal z -stacks and discretized into 100 μm sections away from the defect. Across at least 7 different samples, we observed cell invasion over 30 μm deep into the col-I matrix around the defect (averaged within $\sim 200 \mu\text{m}$). These invasion depths reduced away from the defect (Fig. 6C); yet, we found $\sim 10 \mu\text{m}$ deep invasion up

to 2 mm distance away from the defect (Fig. 6B,C). Averaged over the area at any given distance from the defect, we found that over 2000 cells/mm² invaded at least 5 μm deep, while ~100 cells/mm² were able to reach invasion depths of more than 35 μm (Fig. 6D).

By imaging for actin and vimentin, we found that the invaded cells showed robust expressions of actin fibers and vimentin, indicating EMT induction and mechanoactivation, across varying depths of invasion and distance away from the defect (Figs. 6E-G). Cells that invaded more than 15 μm deep into the 3D col-I matrix showed tube-like formations (Fig. 6G; top row, left panels). In comparison, cells closer to the monolayer, i.e., smaller invasion depth, invaded in the form of larger sheets and clusters (Fig. 6G; top row, right panels). Since earlier experiments in 2D showed that a defect is necessary for EMT stimulation on soft substrates and MMP9 inhibition disables EMT, we expected a similar outcome in these multi-layered gels. Indeed, in this 3D gel system, the systems without defects and those with MMP-inhibited cells showed negligible invasion (Figs. 6D,S11; Movies S5,S6). To verify that the col-I matrix remains intact around the defect, we stained and imaged for col-I and found robust col-I expression all around the invading cell population (Fig. S12).

4. Discussion

Our findings reveal that physical defects in the BM matrix can initiate disease-like cellular transformation in the form of EMT and invasion. Thus, the known BM degradation caused by the pathogenic transformation of cells through acquired EMT signatures might not be a one way process. Instead, physical composition of the BM matrix plays a more proactive role in triggering the disease-aiding EMT and motility in normal epithelial cells.

Through mechanotransductive signaling, stress fiber formation and morphological adaptation,^{13-15,19,43} cellular EMT and invasion can respond to the stiffness and topography of their microenvironments,^{15-17,28,43-47} which themselves undergo dramatic mechanical changes in cancer and fibrosis.^{31,43,48-50} In particular, the basement membrane around tumors *in situ* undergoes degradation and becomes heterogeneous as cells exhibit mesenchymal signatures and tumor invasiveness increases.^{24,51,52} Here, we have attempted to deconstruct this intricate coupling between EMT and BM heterogeneities in pathogenesis. We show that a preexisting defect in a BM-like soft matrix with a col-IV layer causes broad mesenchymal signatures in a sheet of normal MCF10A cells (Fig. 2). These increases propagate through the monolayer over time, continuing to induce EMT further and further away from the defect (Fig. 5). Given that edges in the matrix introduced due to microfabricated confinement¹⁷ or micropatterned ligand patches¹⁸ are known to induce EMT, we expected that the loss of cell-cell cohesion near the open boundary created by the defect would enhance cellular mechanoactivation, which in turn would lead to cell-cell dissociation and EMT. Although we did find enhanced EMT signatures around the BM matrix defect, surprisingly the RhoA activation and stress fiber formation remained low after 3 days of culture (Fig. 3). We also found the defect did not create an artificial space that cells could exploit for increased proliferation (Fig. S13). Thus, unlike the earlier cases of topographic confinement or ligand patterning,^{17,18} the physical boundary created by the defect was not enough to increase cellular mechanoactivation. Instead, the EMT was triggered by the degraded col-IV, which in turn enhanced cellular mechanoactivation. In retrospect, given that these experiments were conducted on a soft matrix, it is not surprising that the cells maintain low mechanoactivation and stress fiber formation regardless of a physical defect until EMT induction.

In another mode of matrix-regulated EMT, epithelial cells cultured on stiff matrix quickly undergo cellular mechanoactivation, marked by higher stress fiber formation and morphological elongation, developing somewhat concurrently with the EMT, as shown earlier^{13-17,19} and reproduced here on a collagen IV-laden matrix (Fig. 3). In the case of defective BM matrix, stress fiber formation increases after the EMT induction over 6 days of culture. Thus, since the BM discontinuities led to cellular EMT even on a soft matrix and without stress fiber formation in the first 3 days (Figs. 2, 3), we concluded the main cause of BM defect-induced EMT is not cellular mechanoactivation. We observed that col-IV expression near the defect was lower than the control conditions, which indicated that the degraded col-IV fibrils around the defect might directly initiate an EMT response. Consistent with this hypothesis, it has been previously shown that external introduction of col-IV fibrils into the culture media can induce EMT-like signatures in mammary epithelial cells.⁵³ Indeed, when the col-IV degradation was disabled through MMP9 inhibition, the EMT signatures around the matrix defect vanished. Notably, since the EMT on the stiff matrix persists even after MMP9 inhibition, it can be assumed that the used pharmacological inhibitor is not a universal EMT blocker.

Our results point to the following framework for BM defect-induced EMT – a tear in the col-IV network allows the cellular MMP9 to access col-IV binding sites and stimulate degradation; the degraded col-IV fibrils initiate EMT signaling within 3 days; the EMT induction propagates through the epithelial layer in a spatiotemporal manner; the defect-induced EMT and ECM stiffness can both independently enhance cellular mechanoactivation; the EMT-induced cellular mechanoactivation could provide a positive feedback for EMT. To further understand this complex feedback among EMT, cellular mechanoactivation, matrix stiffness, discontinuities, and col-IV concentration, we constructed a novel computational model that

integrates biochemical (col-IV based) and biomechanical (stiffness based) contributions towards spatiotemporal EMT propagation. Although previous discrete cell models^{54,55} include intercellular signaling in cell populations, they do not explicitly account for actomyosin forces, adhesions, and cell deformations, which limits the mechanical feedback and mechanosensing among cell neighbors. Our novel multiscale model captures subcellular signaling, cell-level deformations, and feedback across an epithelial cell network, all operating at different spatiotemporal scales. After validation of the key rate constants in the model against the experimentally measured EMT markers, we simulated EMT and cellular mechanoactivation within epithelial layers on soft, soft-defect, and stiff matrices. The fidelity of simulations with experimental findings indicates that the presented model could predict new situations that may not be readily accessible through simple experiments.

In physiological settings, cellular EMT and mechanoactivation leads to cell migration and invasion through the surrounding tissue environments. We have shown that the EMT-based cellular transformation due to BM matrix defect triggers wide-ranging changes in the cells, including activated actin-myosin force machinery. On a defective collagen IV-laden 3D collagen I matrix, we found that the defect-induced EMT enabled the MCF10A cells to undergo EMT and invade through the collagen I matrix. Thus, physical defects in a BM-like matrix do not merely induce transient or benign forms of EMT and mechanoactivation signatures. Instead, these defect-induced cellular changes have real consequences for *in vivo* situations of BM degradation and stromal invasion, as clear from the measured distant 3D cellular invasion within 6 days of culture (Fig. 6). After MMP9 inhibition, both the EMT induction and cellular invasion completely stopped. In organ level experiments, overexpression of MMPs, through macrophages and fibroblasts, has been shown to induce EMT.⁵⁶⁻⁵⁸ In a new advance, we have discovered that

normal epithelial cells can exploit preexisting defects in a soft BM matrix to degrade col-IV through MMP9 and attain disease-progressing phenotypes of EMT and 3D invasion. It is already known that MMP9 activity in immune and cancer cells potentiates lung metastasis,⁵⁹ promotes tumor vascularization,⁶⁰ and predicts breast cancer brain metastasis.⁶¹ Additionally, upregulated MMP1 and MMP2 are known to degrade collagen-rich environments,^{2,62} including the basement membrane,⁶³ and accelerate tumor invasion. Our findings provide further indication that MMP9 activity in particular may play a broad role in BM matrix degradation, which would further promote tumor cell invasion and stromal matrix remodeling through MMP1/2 activity.

Given that the BM microenvironment is composed of many proteins, including laminin,^{6,8} the future *in vitro* BM models should go beyond the col-IV coating for improved *in vivo* impact of our findings of BM defect-induced cellular response. Rise in ligand density has been shown to diminish EMT even on stiff substrate through upregulation of integrin $\beta 4$ and Rac1 activity.⁶⁴ Thus, it is possible that additional BM proteins might enhance cell-BM adhesions and reduce the defect-induced EMT invasion. Since laminin in particular has also been shown to play a critical role in breast cancer metastasis,^{64,65} its presence in the BM matrix might provide better insights into cell invasion around defective BM matrix. With progressively increasing complexity, the BM-mimicking *in vitro* models are likely to provide a more accurate understanding of broad cellular response to mechanical defects and heterogeneities in the BM matrix.

Acknowledgements

This work was supported by the Washington University Faculty Startup Fund and in part by grants from the National Science Foundation (CAREER Award 1454016) and the Edward Mallinckrodt, Jr. Foundation (New Investigator Award) to AP.

References

1. Nistico P, Bissell MJ, Radisky DC. Epithelial-mesenchymal transition: general principles and pathological relevance with special emphasis on the role of matrix metalloproteinases. *Cold Spring Harbor perspectives in biology* **4**, (2012).
2. Rowe RG, Weiss SJ. Navigating ECM Barriers at the Invasive Front: The Cancer Cell-Stroma Interface. *Annu. Rev. Cell Dev. Biol.* **25**, 567-595 (2009).
3. Sherwood DR. Cell invasion through basement membranes: an anchor of understanding. *Trends Cell Biol.* **16**, 250-256 (2006).
4. Yurchenco PD. Basement membranes: cell scaffoldings and signaling platforms. *Cold Spring Harbor perspectives in biology* **3**, (2011).
5. Hagedorn EJ, Sherwood DR. Cell invasion through basement membrane: the anchor cell breaches the barrier. *Current opinion in cell biology* **23**, 589-596 (2011).
6. Kalluri R. Basement membranes: structure, assembly and role in tumour angiogenesis. *Nature reviews. Cancer* **3**, 422-433 (2003).
7. Carraro DM, Elias EV, Andrade VP. Ductal carcinoma in situ of the breast: morphological and molecular features implicated in progression. *Biosci Rep* **34**, (2014).
8. Kelley LC, Lohmer LL, Hagedorn EJ, Sherwood DR. Traversing the basement membrane in vivo: A diversity of strategies. *The Journal of Cell Biology* **204**, 291 (2014).
9. Kalluri R. Discovery of Type IV Collagen Non-collagenous Domains as Novel Integrin Ligands and Endogenous Inhibitors of Angiogenesis. *Cold Spring Harbor Symposia on Quantitative Biology* **67**, 255-266 (2002).
10. Timpl R, Wiedemann H, Van Delden V, Furthmayr H, KÜHn K. A Network Model for the Organization of Type IV Collagen Molecules in Basement Membranes. *European Journal of Biochemistry* **120**, 203-211 (1981).

11. Stuart K, Paderi J, Snyder PW, Freeman L, Panitch A. Collagen-binding peptidoglycans inhibit MMP mediated collagen degradation and reduce dermal scarring. *PLoS One* **6**, e22139 (2011).
12. Rowe RG, Weiss SJ. Breaching the basement membrane: who, when and how? *Trends Cell Biol* **18**, 560-574 (2008).
13. Leight JL, Wozniak MA, Chen S, Lynch ML, Chen CS. Matrix rigidity regulates a switch between TGF-beta1-induced apoptosis and epithelial-mesenchymal transition. *Molecular biology of the cell* **23**, 781-791 (2012).
14. Lee K, Chen QK, Lui C, Cichon MA, Radisky DC, Nelson CM. Matrix compliance regulates Rac1b localization, NADPH oxidase assembly, and epithelial-mesenchymal transition. *Molecular biology of the cell* **23**, 4097-4108 (2012).
15. Wei SC, *et al.* Matrix stiffness drives epithelial-mesenchymal transition and tumour metastasis through a TWIST1-G3BP2 mechanotransduction pathway. *Nat Cell Biol*, (2015).
16. Pathak A. Scattering of Cell Clusters in Confinement. *Biophysical journal* **111**, 1496-1506 (2016).
17. Nasrollahi S, Pathak A. Topographic confinement of epithelial clusters induces epithelial-to-mesenchymal transition in compliant matrices. *Scientific reports* **6**, 18831 (2016).
18. Gomez Esther W, Chen Qike K, Gjorevski N, Nelson Celeste M. Tissue geometry patterns epithelial-mesenchymal transition via intercellular mechanotransduction. *Journal of Cellular Biochemistry* **110**, 44-51 (2010).
19. Brown AC, Fiore VF, Sulchek TA, Barker TH. Physical and chemical microenvironmental cues orthogonally control the degree and duration of fibrosis-associated epithelial-to-mesenchymal transitions. *The Journal of pathology* **229**, 25-35 (2013).
20. Lovisa S, *et al.* Epithelial-to-mesenchymal transition induces cell cycle arrest and parenchymal damage in renal fibrosis. *Nat Med* **21**, 998-1009 (2015).

21. Nakaya Y, Sukowati EW, Wu Y, Sheng GJ. RhoA and microtubule dynamics control cell-basement membrane interaction in EMT during gastrulation. *Nat Cell Biol* **10**, 765-775 (2008).
22. Van Hoof J, Harrisson F. Interaction between epithelial basement membrane and migrating mesoblast cells in the avian blastoderm. *Differentiation* **32**, 120-124 (1986).
23. Petersen OW, Ronnov-Jessen L, Howlett AR, Bissell MJ. Interaction with basement membrane serves to rapidly distinguish growth and differentiation pattern of normal and malignant human breast epithelial cells. *Proc Natl Acad Sci U S A* **89**, 9064-9068 (1992).
24. Esposito NN, Dabbs DJ, Bhargava R. Are encapsulated papillary carcinomas of the breast in situ or invasive? A basement membrane study of 27 cases. *Am J Clin Pathol* **131**, 228-242 (2009).
25. Nasrollahi S, Walter C, Loza AJ, Schimizzi GV, Longmore GD, Pathak A. Past matrix stiffness primes epithelial cells and regulates their future collective migration through a mechanical memory. *Biomaterials* **146**, 146-155 (2017).
26. Pathak A, Kumar S. Independent regulation of tumor cell migration by matrix stiffness and confinement. *Proc. Natl. Acad. Sci. U.S.A.* **109**, 10334-10339 (2012).
27. Fischer RS, Myers KA, Gardel ML, Waterman CM. Stiffness-controlled three-dimensional extracellular matrices for high-resolution imaging of cell behavior. *Nature protocols* **7**, 2056-2066 (2012).
28. Pathak A, Kumar S. Transforming potential and matrix stiffness co-regulate confinement sensitivity of tumor cell migration. *Integr. Biol.* **5**, 1067-1075 (2013).
29. Debnath J, Muthuswamy SK, Brugge JS. Morphogenesis and oncogenesis of MCF-10A mammary epithelial acini grown in three-dimensional basement membrane cultures. *Methods* **30**, 256-268 (2003).
30. Livak KJ, Schmittgen TD. Analysis of Relative Gene Expression Data Using Real-Time Quantitative PCR and the $2^{-\Delta\Delta CT}$ Method. *Methods* **25**, 402-408 (2001).

31. Walter C, *et al.* Increased Tissue Stiffness in Tumors from Mice with Neurofibromatosis-1 Optic Glioma. *Biophysical journal* **112**, 1535-1538 (2017).
32. Hardin J, Walston T. Models of morphogenesis: the mechanisms and mechanics of cell rearrangement. *Current opinion in genetics & development* **14**, 399-406 (2004).
33. Mirams GR, *et al.* Chaste: an open source C++ library for computational physiology and biology. *PLoS Comput Biol* **9**, e1002970 (2013).
34. Drasdo D. Buckling Instabilities of One-Layered Growing Tissues. *Physical Review Letters* **84**, 4244-4247 (2000).
35. Farhadifar R, Roper JC, Aigouy B, Eaton S, Julicher F. The influence of cell mechanics, cell-cell interactions, and proliferation on epithelial packing. *Current biology : CB* **17**, 2095-2104 (2007).
36. Canel M, Serrels A, Frame MC, Brunton VG. E-cadherin-integrin crosstalk in cancer invasion and metastasis. *J Cell Sci* **126**, 393-401 (2013).
37. de Rooij J, Kerstens A, Danuser G, Schwartz MA, Waterman-Storer CM. Integrin-dependent actomyosin contraction regulates epithelial cell scattering. *J Cell Biol* **171**, 153-164 (2005).
38. Chalhoub N, Baker SJ. PTEN and the PI3-kinase pathway in cancer. *Annual review of pathology* **4**, 127-150 (2009).
39. Ren Y, Zhou X, Qi Y, Li G, Mei M, Yao Z. PTEN activation sensitizes breast cancer to PI3-kinase inhibitor through the beta-catenin signaling pathway. *Oncology reports* **28**, 943-948 (2012).
40. Zeng ZS, Cohen AM, Guillem JG. Loss of basement membrane type IV collagen is associated with increased expression of metalloproteinases 2 and 9 (MMP-2 and MMP-9) during human colorectal tumorigenesis. *Carcinogenesis* **20**, 749-755 (1999).
41. Buxboim A, Ivanovska IL, Discher DE. Matrix elasticity, cytoskeletal forces and physics of the nucleus: how deeply do cells 'feel' outside and in? *J Cell Sci* **123**, 297-308 (2010).

42. Engler AJ, Richert L, Wong JY, Picart C, Discher DE. Surface probe measurements of the elasticity of sectioned tissue, thin gels and polyelectrolyte multilayer films: Correlations between substrate stiffness and cell adhesion. *Surface Science* **570**, 142-154 (2004).
43. Paszek MJ, *et al.* Tensional homeostasis and the malignant phenotype. *Cancer Cell* **8**, 241-254 (2005).
44. Ulrich TA, de Juan Pardo EM, Kumar S. The mechanical rigidity of the extracellular matrix regulates the structure, motility, and proliferation of glioma cells. *Cancer Res.* **69**, 4167-4174 (2009).
45. Sabeh F, Shimizu-Hirota R, Weiss SJ. Protease-dependent versus -independent cancer cell invasion programs: three-dimensional amoeboid movement revisited. *The Journal of Cell Biology* **185**, 11-19 (2009).
46. Beadle C, Assanah MC, Monzo P, Vallee R, Rosenfeld SS, Canoll P. The Role of Myosin II in Glioma Invasion of the Brain. *Molecular biology of the cell* **19**, 3357-3368 (2008).
47. Kun Zhang, *et al.* Mechanical signals regulate and activate SNAIL1 protein to control the fibrogenic response of cancer-associated fibroblasts. *Journal of Cell Science* (**in press**), doi:10.1242/jcs.180539 (2016).
48. McKnight AL, Kugel JL, Rossman PJ, Manduca A, Hartmann LC, Ehman RL. MR Elastography of Breast Cancer: Preliminary Results. *American Journal of Roentgenology* **178**, 1411-1417 (2002).
49. Miyaji K, *et al.* The stiffness of lymph nodes containing lung carcinoma metastases. *Cancer* **80**, 1920-1925 (1997).
50. Baker AM, Bird D, Lang G, Cox TR, Erler JT. Lysyl oxidase enzymatic function increases stiffness to drive colorectal cancer progression through FAK. *Oncogene* **32**, 1863-1868 (2013).
51. Kallioinen M, Autio-Harmainen H, Dammert K, Risteli J, Risteli L. Discontinuity of the Basement Membrane in Fibrosing Basocellular Carcinomas and Basosquamous

- Carcinomas of the Skin: An Immunohistochemical Study with Human Laminin and Type IV Collagen Antibodies. *Journal of Investigative Dermatology* **82**, 248-251 (1984).
52. Kallioinen M, Autio-Harminen H, Dammert K, Risteli J, Risteli L. Discontinuity of the basement membrane in fibrosing basocellular carcinomas and basosquamous carcinomas of the skin: an immunohistochemical study with human laminin and type IV collagen antibodies. *J Invest Dermatol* **82**, 248-251 (1984).
 53. Espinosa Neira R, Salazar EP. Native type IV collagen induces an epithelial to mesenchymal transition-like process in mammary epithelial cells MCF10A. *The International Journal of Biochemistry & Cell Biology* **44**, 2194-2203 (2012).
 54. Vargas DA, Bates O, Zaman MH. Computational model to probe cellular mechanics during epithelial-mesenchymal transition. *Cells, tissues, organs* **197**, 435-444 (2013).
 55. Kumar S, Das A, Sen S. Extracellular matrix density promotes EMT by weakening cell-cell adhesions. *Molecular bioSystems* **10**, 838-850 (2014).
 56. Radisky ES, Radisky DC. Matrix metalloproteinase-induced epithelial-mesenchymal transition in breast cancer. *Journal of mammary gland biology and neoplasia* **15**, 201-212 (2010).
 57. Lin CY, *et al.* Matrix metalloproteinase-9 cooperates with transcription factor Snail to induce epithelial-mesenchymal transition. *Cancer science* **102**, 815-827 (2011).
 58. Tan TK, *et al.* Macrophage matrix metalloproteinase-9 mediates epithelial-mesenchymal transition in vitro in murine renal tubular cells. *Am J Pathol* **176**, 1256-1270 (2010).
 59. Hiratsuka S, *et al.* MMP9 induction by vascular endothelial growth factor receptor-1 is involved in lung-specific metastasis. *Cancer Cell* **2**, 289-300 (2002).
 60. Mehner C, Hockla A, Miller E, Ran S, Radisky DC, Radisky ES. Tumor cell-produced matrix metalloproteinase 9 (MMP-9) drives malignant progression and metastasis of basal-like triple negative breast cancer. *Oncotarget* **5**, 2736-2749 (2014).

61. Mendes O, Kim H-T, Stoica G. Expression of MMP2, MMP9 and MMP3 in Breast Cancer Brain Metastasis in a Rat Model. *Clinical & experimental metastasis* **22**, 237-246 (2005).
62. Wolf K, *et al.* Physical limits of cell migration: Control by ECM space and nuclear deformation and tuning by proteolysis and traction force. *The Journal of Cell Biology* **201**, 1069-1084 (2013).
63. Ota I, Li X-Y, Hu Y, Weiss SJ. Induction of a MT1-MMP and MT2-MMP-dependent basement membrane transmigration program in cancer cells by Snail1. *Proc. Natl. Acad. Sci. U.S.A.* **106**, 20318 (2009).
64. Chaudhuri O, *et al.* Extracellular matrix stiffness and composition jointly regulate the induction of malignant phenotypes in mammary epithelium. *Nature materials* **13**, 970-978 (2014).
65. Benton G, Crooke E, George J. Laminin-1 induces E-cadherin expression in 3-dimensional cultured breast cancer cells by inhibiting DNA methyltransferase 1 and reversing promoter methylation status. *The FASEB Journal* **23**, 3884-3895 (2009).

FIGURES

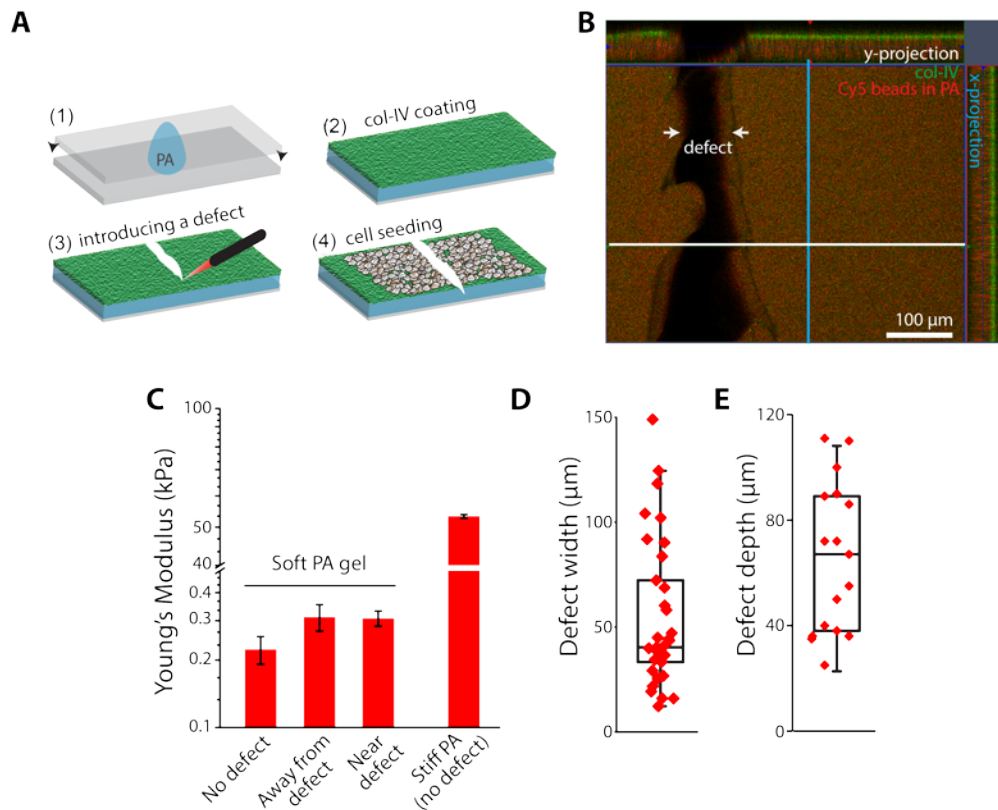


Figure 1. EMT induction around physical defects in soft BM-like col-IV matrix. (A) In four steps, soft PA gel is fabricated, col-IV layer is deposited, a defect is introduced in the form of a tear, and MCF10A cells are seeded. (B) Orthogonal projections of a representative immunofluorescent image with x - and y -profiles (blue and white lines, respectively) of the imposed defect in col-IV coated PA gels using col-IV antibody (Abcam) with Alexa Fluor 488 ELISA and 0.5 μm diameter fluorescent beads, respectively. (C) Average Young's Modulus measured by AFM of soft PA gels prior to the introduction of defect (no defect), near the defect, and away from defect, as well as homogeneous stiff PA gels. (D) Average defect width measured via immunofluorescent images, as shown in (B). Box represents 25-75 percent of data. Whiskers represent outliers. Error bars = SEM. (E) Average defect depth measured via immunofluorescent images, as shown in (B). Box represents 25-75 percent of data. Whiskers represent outliers. Error bars = SEM.

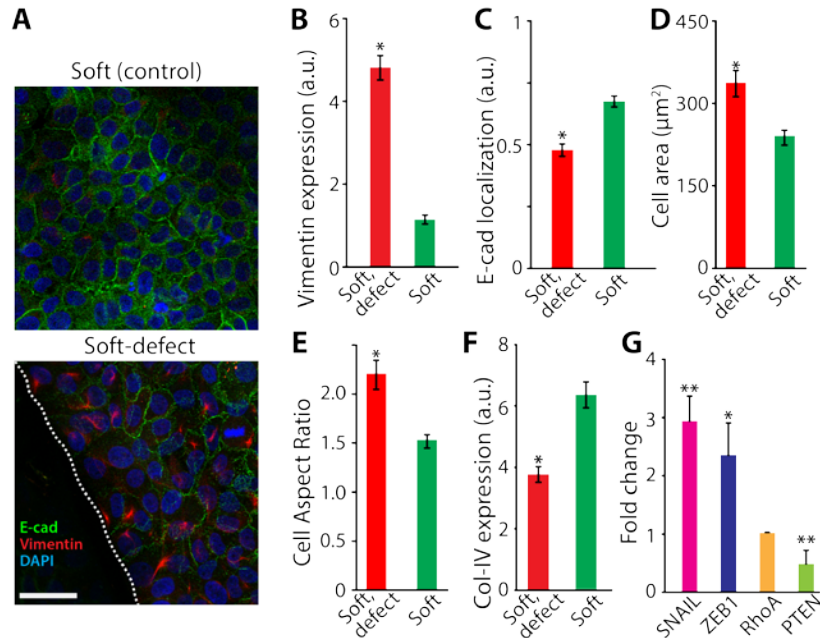


Figure 2. EMT induction after 3 days of epithelial cell culture around physical defects in soft BM-like col-IV matrix. (A) Representative immunofluorescence images of E-cad (green), vimentin (red), and DAPI (blue) in MCF10A cell monolayers cultured for 3 days on soft (0.5 kPa) PA gels with and without (homogeneous controls) defect. Scale bar=50 μm . (B) Average vimentin expression, (C) membrane localization of E-cad, (D) spreading area of individual cells within the monolayer, (E) cell aspect ratio, and (F) average col-IV expression. $N > 30$. (G) qPCR measurements of SNAIL, ZEB1, RhoA, and PTEN levels relative to GAPDH controls, plotted as fold change ($\Delta\Delta\text{ct}$) compared to the levels on soft control matrices. Error bars = SEM. * $p < 0.01$, and ** $p < 0.001$ compared to soft substrates.

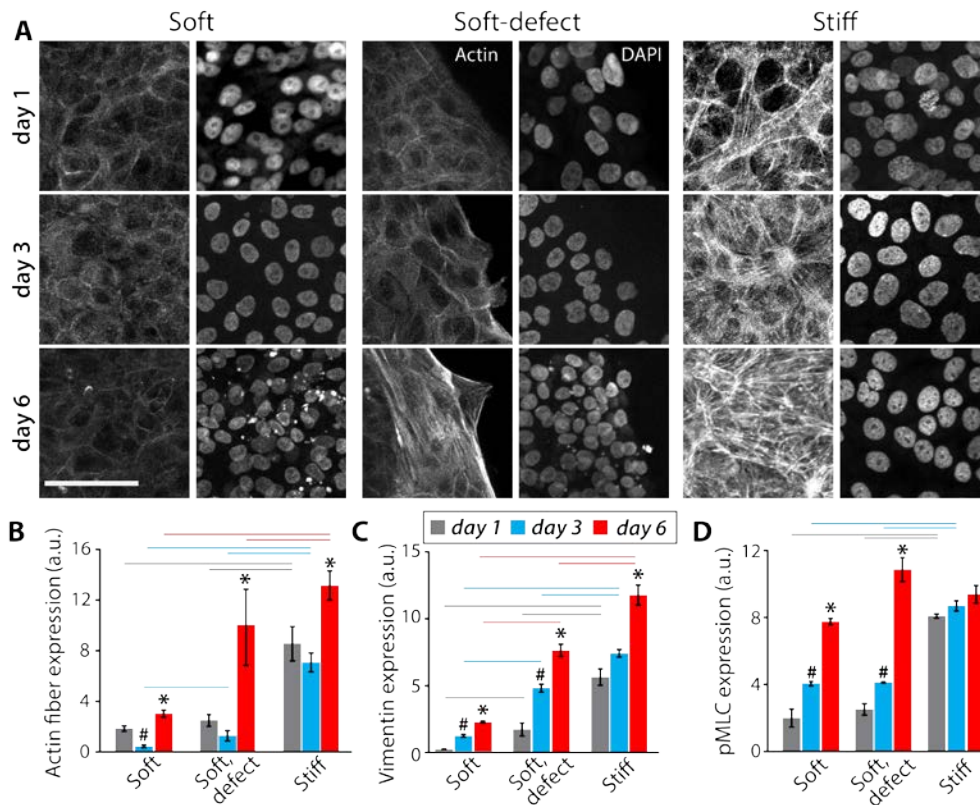


Figure 3. Defect-induced EMT precedes stress fiber formation, but stiffness-induced EMT and stress fibers evolve concurrently. (A) Representative immunofluorescence images of F-actin (red) and DAPI (blue) in MCF10A monolayers on soft, soft-defect, and stiff PA gels after 1, 3, or 6 days in culture. Scale bar=50 μm . Average expressions of (B) vimentin, (C) actin fibers, and (D) pMLC across the three ECM conditions after 1, 3, and 6 days. $N > 20$. Error bars = SEM. *,# $p < 0.01$ compared to soft control ECM. Horizontal lines above bars indicate $p < 0.01$ between the indicated substrate conditions.

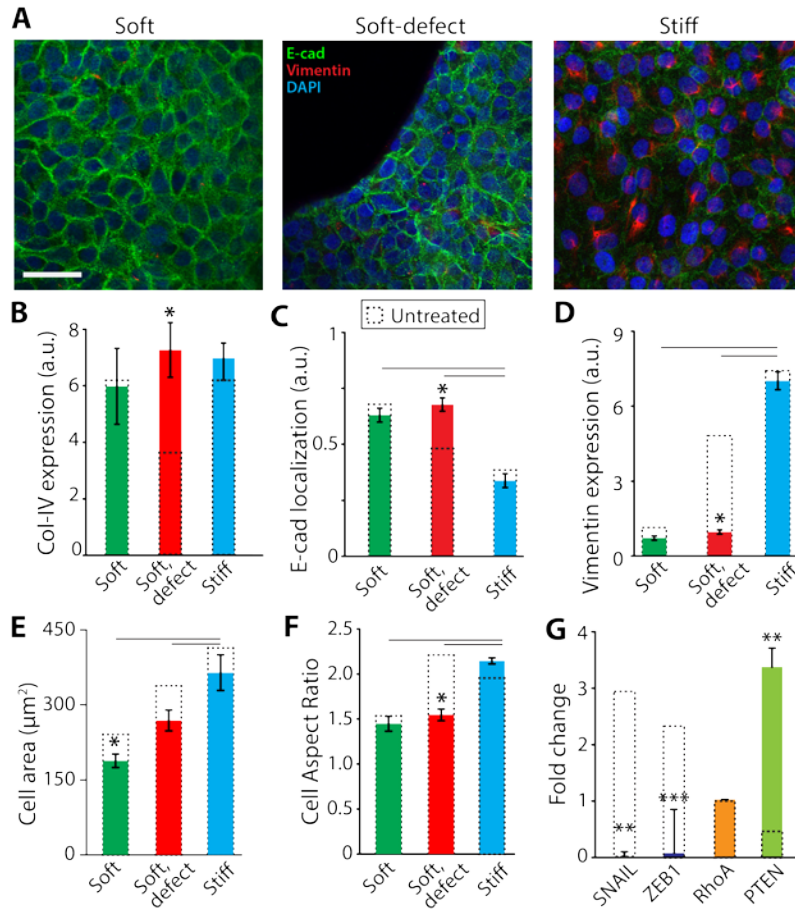


Figure 4. MMP9 inhibition blocks defect-induced EMT by disabling col-IV degradation. (A) Representative immunofluorescence images of E-cad, vimentin, and DAPI in MCF10A cell monolayer after treatment with MMP9 inhibitor on soft, soft-defect, and stiff PA gels. Scale bar=50 μm . Average expressions of (B) col-IV, (C) membrane-localized E-cad, (D) vimentin, and average (E) spreading area and (F) aspect ratio of MMP9-inhibited cells. $N > 30$. * $p < 0.01$ compared to untreated cells on the same substrate (dashed boxes). Horizontal lines above bars indicate $p < 0.01$ between the indicated substrate conditions. (G) Fold change from qPCR measurements of SNAIL, ZEB1, RhoA, and PTEN levels relative to GAPDH control. Gray dashed boxes represent values for wildtype (without drug treatment) cells. Error bars = SEM. * $p < 0.01$, ** $p < 0.001$, and *** $p < 0.001$ compared to soft control ECMs.

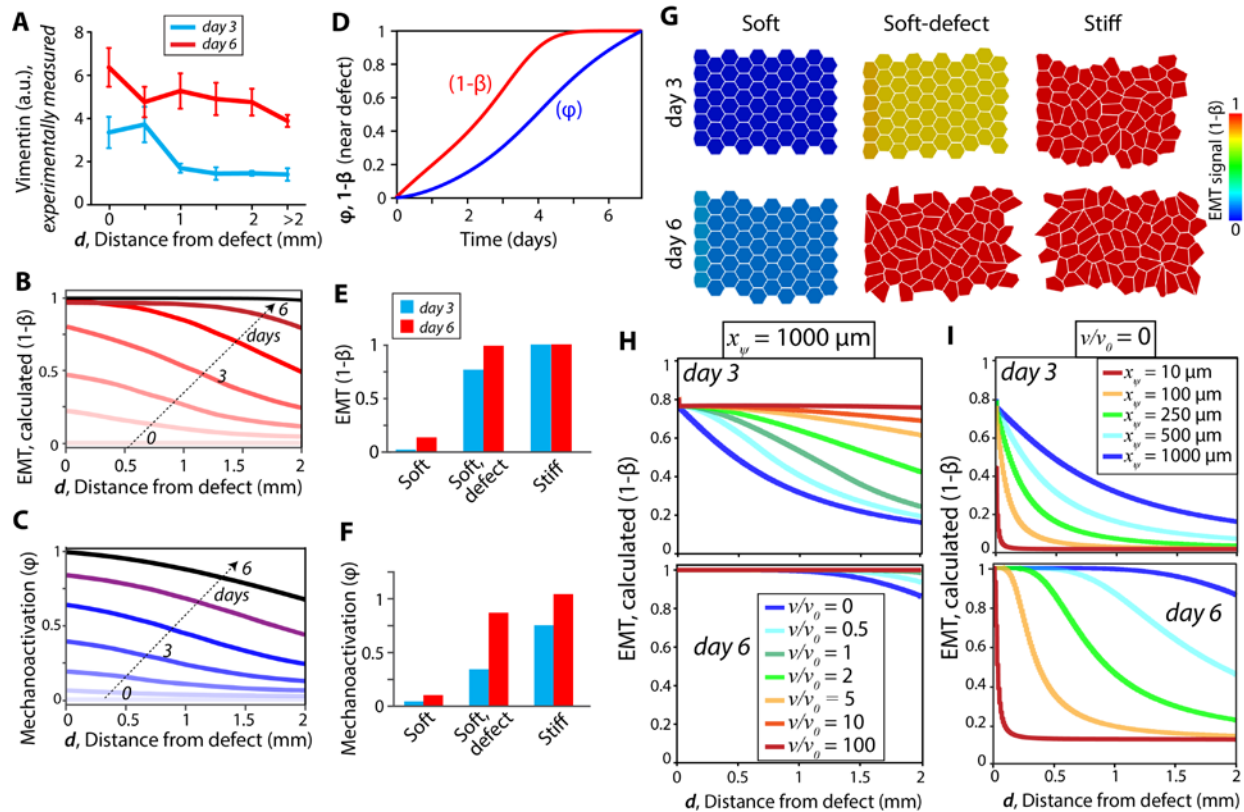


Figure 5. Simulations of EMT progression through cell monolayers on matrices with and without discontinuity. (A) Average vimentin expression measured in experiments on soft-defect matrices, plotted as a function of distance from the defect after days 3 and 6 of culture. (B) EMT signal, $1-\beta$, and (C) mechanoactivation signal, ϕ , calculated through simulations, plotted over distance from the coded discontinuity in the matrix and over 6 days of simulation time. (D) Predicted temporal evolution of EMT and mechanoactivation signals near the defect. Averaged (E) EMT and (F) mechanoactivation signals, and (G) snapshots of cellular morphology from simulations run on soft-homogeneous, soft with discontinuity, and stiff-homogeneous matrix conditions (see the corresponding Movies S1-3). Plots of EMT signal, $1-\beta$, after 3 and 6 days for (H) varying v/v_0 and $x_\psi=1$ mm, and (I) varying x_ψ and $v/v_0=1$.

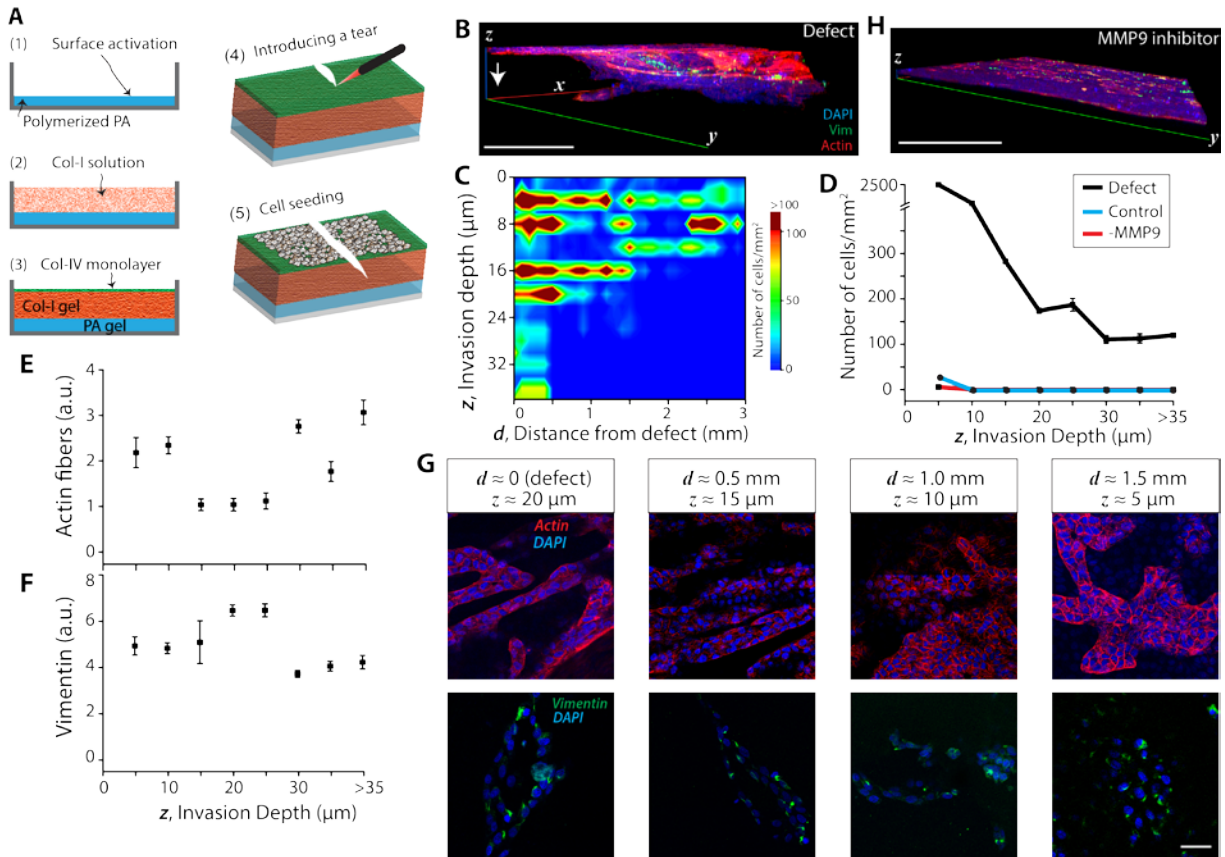
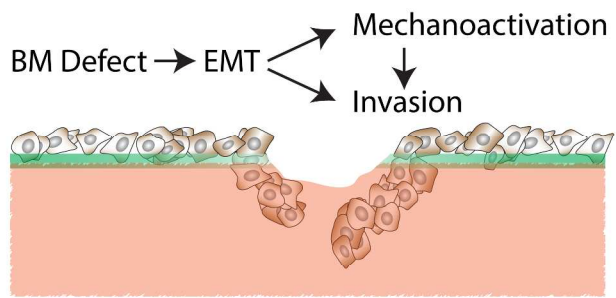


Figure 6. Defect-induced cellular EMT and mechanoactivation cause 3D invasion. (A) Schematic describing the fabrication of a multi-layered BM-stroma-mimicking scaffold with soft PA gels, 3D collagen I matrix, and a coating of col-IV. (B) Volumetric reconstruction of confocal immunofluorescence image z-stacks of actin, vimentin and DAPI showing the invasion of cells into this layered gel system with an introduced defect. Scale bar=50 μm . (C) Heatmap showing average number of cells at a given invasion depth, z, and distance from the defect, d. Quantification of (D) average number of invading cells per unit area, and (E) average vimentin expression and (F) average actin fibers versus invasion depth, normalized per unit area containing cells. Error bars = SEM. (G) Representative images showing the morphology and distribution of invading cell clusters through immunofluorescence imaging of actin, vimentin, and DAPI at various invasion depths (z) and distance from the defect (d). Scale bar = 50 μm . (H) Volumetric reconstruction confocal z-stacks showing negligible invasion of MMP9-inhibited cells around the defect. Scale bar=500 μm .



Normal epithelial cells can exploit physical defects in the basement membrane matrix to undergo disease-like cellular transformations.